Karbala International Journal of Modern Science

Manuscript 3427

Influence of variable climate on mechanical properties of composite materials: an experimental study

Alexandra Tazhibaeva

Safaa M.R.H. Hussein

Mikhail Kuznetsov

Farid Shakirzyanov

Nikita Kharin

See next page for additional authors

Influence of variable climate on mechanical properties of composite materials: an experimental study

Abstract

This study investigates the degradation of carbon fiber-reinforced plastic composites, fabricated via non-autoclave molding, under tropical climatic conditions across three regions over three years. Forty specimens (10 control, 30 exposed) with 2x2 twill weave and 0°/90° fiber orientation were subjected to tensile and compressive testing, microscopy, and X-ray computed tomography. Control specimens established baseline properties, while exposed specimens underwent three-year weathering. Statistical and principal component analyses revealed significant mechanical degradation, with tensile strength decreasing by up to 16.1% (p

Keywords

polymer composite materials; UV radiation; tropical climate; mechanical degradation; non-autoclave molding; envi-ronmental exposure; carbon fiber-reinforced plastic

Authors

Alexandra Tazhibaeva, Safaa M.R.H. Hussein, Mikhail Kuznetsov, Farid Shakirzyanov, Nikita Kharin, Igor Muravyev, Timur Agliullin, Gulshat Saleeva, Victor Mitryakin, Oleg Morozov, and Oskar Sachenkov

RESEARCH PAPER

Influence of Variable Climate on Mechanical Properties of Composite Materials: An Experimental Study

Alexandra Tazhibaeva [a], Safaa M.R.H. Hussein [b], Mikhail Kuznetsov [a], Farid Shakirzyanov [c], Nikita Kharin [c], Igor Muravyev [d], Timur Agliullin [d], Gulshat Saleeva [e], Victor Mitryakin [a], Oleg Morozov [d,*], Oskar Sachenkov [c,f]

[a] Department of Machines Science and Engineering Graphics, Kazan National Research Technical University named after A.N. Tupolev − KAI, Kazan, Russian Federation
[b] University of Karbala, Karbala, Iraq
[c] Institute of Mathematics and Mechanics, Kazan Federal University, Kazan, Russian Federation
[d] Department of Radiophotonics and Microwave Technologies, Kazan National Research Technical University named after A.N. Tupolev − KAI, Kazan, Russian Federation
[e] Orthopedic Dentistry Department, Kazan State Medical University, Kazan, Russian Federation
[f] Federal Research Center "Kazan Scientific Center of Russian Academy of Sciences", Kazan, Russian Federation

Abstract

This study investigates the degradation of carbon fiber-reinforced plastic composites, fabricated via non-autoclave molding, under tropical climatic conditions across three regions over three years. Forty specimens (10 control, 30 exposed) with 2 × 2 twill weave and 0°/90° fiber orientation were subjected to tensile and compressive testing, microscopy, and X-ray computed tomography. Control specimens established baseline properties, while exposed specimens underwent three-year weathering. Statistical and principal component analyses revealed significant mechanical degradation, with tensile strength decreasing by up to 16.1 % ($p < 0.05$), compressive strength by 20.4 % ($p < 0.05$), and tensile modulus increasing by 11.7 % ($p < 0.05$). Microscopy showed matrix discoloration, microcracks, and fiber depigmentation, particularly in high UV-A coastal zones. UV-A and humidity were identified as primary degradation drivers, with UV-B affecting elastic modulus. Topological analysis via birth-death diagrams confirmed structural changes correlated with UV-A and UV-B intensity. Heterogeneous materials are widely used in various applications. These findings underscore the vulnerability of non-autoclave composite to tropical climates and advocate for UV-resistant coatings or matrix modifications to enhance durability.

Keywords: Polymer composite materials, UV radiation, Tropical climate, Mechanical degradation, Non-autoclave molding, Environmental exposure, Carbon fiber-reinforced plastic

1. Introduction

Heterogeneous materials are widely used in various applications [1,2]. Innovative composite material (CM) fabrication techniques and advances in additive technologies (AT) have redefined traditional material concepts, enabling the integration of heterogeneous materials across industries [3]. Thus, CM are widely used in aerospace [4], automotive [5], space [6], energy [7] and other advanced industries [8,9]. Products fabricated with AT are used in medicine [10−12], construction [13] and aircraft construction [14].

However, despite the extensive research and widespread use of heterogeneous materials, inherent limitations remain due to difficulties in

Received 19 May 2025; revised 24 July 2025; accepted 30 July 2025.
Available online 15 September 2025

* Corresponding author.
E-mail address: ogmorozov@kai.ru (O. Morozov).

https://doi.org/10.33640/2405-609X.3427

their manufacturing processes and operating conditions. For example, components made by additive manufacturing, autoclave or non-autoclave curing often have internal porosity, which can degrade their performance [15–17]. Porosity in heterogeneous materials is usually evaluated by X-ray computed tomography and ultrasound studies [16–19]. However, their mechanical properties are often inconsistent due to inherent variations in the manufacturing process, resulting in a significant variation in experimental results. PCMs are characterized by low density, which contributes to their high strength-to-weight ratio. However, non-autoclave curing methods for the fabrication of CMs do not allow the creation of complex geometric structures such as lattice frameworks or highly porous structures due to inherent process limitations [20–22]. PCMs are also more susceptible to environmental influences – UV radiation, moisture and thermal fluctuations – compared to AT-derived metals [23,24]. Consequently, understanding the long-term effects of these environmental factors on PCM performance is critical to ensure material reliability.

Ultraviolet (UV) radiation from sunlight is a major environmental factor affecting the mechanical properties of composite materials [25–27]. This radiation alters the chemical structure of polymer bonds in PCM, although its penetration depth is usually limited to the micrometer scale, indicating that the degradation occurs mainly at the surface [28–30]. This surface failure can lead to the formation of microcracks that can promote moisture penetration. In combination with thermal cycling [31], localized stress concentrations develop, promoting crack propagation and compromising the material's structural integrity.

Experimental studies of composites exposed to ultraviolet radiation and moisture not only clarify the degradation mechanisms, but also make it possible to optimize the manufacturing and subsequent processing technologies of these materials [32,33]. Such improvements can ultimately improve the physical and mechanical properties of PCMs, ensuring their long-term structural reliability and safety in real-world applications.

Thus, the novelty of this study lies in its long-term (three-year) evaluation of non-autoclave-molded composites under diverse tropical climatic conditions, integrating mechanical testing, microscopy, X-ray computed tomography, and advanced topological data analysis. Specifically, the application of topological analysis through birth-death diagrams derived from X-ray CT data represents a groundbreaking approach, enabling a detailed correlation between structural changes and mechanical degradation at a voxel-level resolution.

This study focuses on non-autoclave-molded composites, aligning with prior work on epoxy-based composites [25,26] and non-autoclave fabrication [16,20]. However, while previous studies primarily rely on mechanical testing to assess environmental degradation, they often overlook complementary structural analyses. Our research distinguishes itself by integrating mechanical testing with microscopy, X-ray computed tomography, and topological data analysis using birth-death diagrams derived from CT data.

2. Materials and methods

2.1. Samples

The study evaluates the impact of tropical climate exposure across three different zones on the structural evolution and mechanical properties of PCMs. For this purpose, two specimen variants were manufactured from carbon fiber-reinforced plastic (CFRP) using a prepreg base and non-autoclave molding techniques. The CFRP specimens were fabricated using ACM 102 prepreg (C200T, epoxy-based) via vacuum-oven molding at 140 ± 5 °C for 3 h under a vacuum pressure of −1 bar. The main properties of the CFRP are summarized in Table 1.

Two different types of specimens were made to evaluate mechanical performance in tensile and compressive loading tests. The test specimens had a carbon fiber structure with a 2x2 twill weave and a density of 200 g/m^2. Each specimen used a fiber orientation of 0°/90°, achieved through a stacking sequence of ten layers, with individual layers having a thickness of 0.2 mm. The tensile specimens were 240 mm long, 20 mm wide and 2 mm thick. The compression test specimens were 80 mm long, 10 mm wide and 4 mm thick. Fig. 1 illustrates the specimen configurations during mechanical testing: (a) tensile and (b) compressive loading setups within the testing machine.

Table 1. Material properties of the CFRP.

Parameter	Value
Tensile strength, MPa	871
Tensile elastic modulus, GPa	71
Compressive strength, MPa	802
Compressive elastic modulus, GPa	60
Prepreg type	ACM 102 (C200T, twill weave)
Resin type	Epoxy
Resin content (wt %)	38–42 %
Fiber volume fraction	58–62 %

A B

Fig. 1. Photos of testing specimens: A − tensile test; B − compressive test.

A total of 40 samples were fabricated. Ten specimens served as control specimens, undergoing mechanical evaluation under laboratory conditions to determine baseline performance. Control specimens were subjected to mechanical testing immediately after fabrication in a controlled laboratory environment at 23 °C and 50 % relative humidity, ensuring baseline properties were evaluated without environmental degradation and enabling valid comparisons with exposed specimens. Thirty specimens (ten for each climatic zone) were allocated to aging studies involving prolonged environmental exposure in three different tropical regions to evaluate degradation mechanisms.

2.2. Mechanical tests

Mechanical properties of the specimens were evaluated using a BISS-50 universal testing machine. The mechanical tests were conducted in accordance with ASTM D3039. The key technical specifications of the equipment, including load frame capacity and control modes, are provided in Table 2.

All specimens were loaded to failure under quasi-static conditions with displacement rate of 2 mm/min.

Table 2. BISS-50 specifications.

Parameter	Value
Maximum load, kN	50
Speed range, mm/min	0.001−500
Accuracy of load measurement, %	±0.5
Resolution of strain gauges, μm	0.1
Readout frequency, kHz	1

The linear zone of stress−strain curves in tensile and compression tests was used to estimate the modulus of elasticity. Linear regression analysis was performed for the elastic zone to establish the stress (σ) − strain (ε) relationship in the following form:

$$\sigma = k \cdot \varepsilon + b, \quad (1)$$

where k is the angular coefficient of the line, b is the free term.

The elastic modulus (E) was calculated as the tangent of the angle (k) of the linear regression fit:

$$E = \tan(k). \quad (2)$$

The ultimate strength (σ_B) was determined by dividing the maximum load (F_{max}) by the initial cross-sectional area (A_0) of the specimen:

$$\sigma_B = \frac{F_{\max}}{A_0}. \quad (3)$$

2.3. Meteorological data

Three climate zones were selected for long-term environmental exposure, each with a distinct climatic profile determined by its geographical local.

Area 1: Tropical maritime climate, moderated by persistent sea breezes despite year-round elevated temperatures. Area 2: Tropical monsoon climate with pronounced wet and dry seasons. Area 3: Tropical savanna climate characterized by consistently high temperatures and minimal seasonal variation.

Specimens were mounted on exposure racks angled at 30° relative to horizon (Fig. 2) and were fully exposed to all climatic factors, including direct precipitation, without any sheltering. This orientation ensured maximal UV radiation dosage while simulating real-world structural loading conditions.

The specimens were exposed to outdoor weathering on test racks for three years (2020−2022). Key climatic parameters including total solar radiation, UV-A/B radiation, total rainfall, and average temperature, humidity, and atmospheric pressure were determined to assess the impact of the tropical environment.

2.4. Microscopy

To evaluate the surface degradation caused by long-term environmental exposure, microscopic analysis of composite specimens was performed using a Levenhuk DTX 700 LCD digital microscope (model 75075). The main characteristics of microscope are summarized in Table 3.

Fig. 2. Stand for samples exposure.

Table 3. Levenhuk DTX 700 specifications.

Parameter	Value
Magnification, multiples	10-300 (digital zoom: 10–1200)
Maximum resolution, Mpix	12
Research method	Light field
Focus, mm	5–7

Representative areas showing structural degradation were identified for each sample. The study included comparative analysis of both the weathered surface and the unexposed reverse side to assess differences in degradation patterns.

2.5. X-ray computed tomography

To assess the impact of climatic factors on the degradation of the composite material's surface, X-ray computed tomography was employed. The scanning of the samples was carried out using the Green X CT scanner (Korea), which was equipped with an X-ray tube featuring an adjustable accelerating voltage between 60 and 99 kV and a current ranging from 4 to 16 mA, with a focal spot size of 0.5 mm according to IEC 60336 standards. All samples were scanned on 94 kV and 13 mA shooting mode. Tensile specimens from each climatic zone were selected as the test samples, and the voxel line size for each scan was set to 0.12 mm.

2.6. Topological data analysis

After scanning, digital twins of the tensile specimens from different climatic zones were obtained (Fig. 3).

During the scanning of the specimens, an edge effect occurs due to the averaging of Hounsfield values in the boundary layers between the material and the external environment. To eliminate the edge effect, the digital twin was cropped based on pre-defined parameters obtained from the Hounsfield histogram by layers. The new material boundaries were defined as follows:

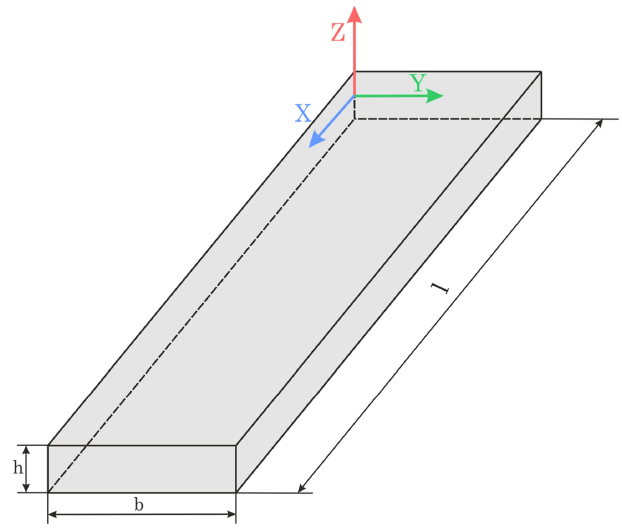

Fig. 3. Scheme of digital twins.

$$x' \in [u;\ l-u],\quad y' \in [v;\ b-u],\quad z' \in \left[-\frac{h}{2}+w;\ \frac{h}{2}-w\right], \tag{4}$$

where x', y', z' are the voxel coordinates in the cropped digital twin, and u, v, w are the number of voxels removed along each axis.

In this study, the number of voxels along the z-axis was 16, with the value of u equal to 1, along the y-axis – 166 and 5, and along the x-axis – 673 and 26, respectively.

For topological data analysis, the resulting computer model was segmented into layers in the xy-plane. The analyzed function was as follows:

$$HU(x'_c, y'_c, z') = f_i(z'), \tag{5}$$

where x_c', y_c' correspond to the value of the considered layer in the $x'z'$-plane.

For the analysis of the obtained optical density change function, Morse filtering was used [34,35]:

$$f(z') = \mu(z') + \epsilon(z'), \tag{6}$$

where $\epsilon(z')$ is the noise and $\mu(z')$ is the Morse function. In the one-dimensional case, the Morse function $g = \mu(z')$ is defined by the set of sublevels R_g as:

$$R_g = \{z' \in R : \mu(z') \leq g\}. \tag{7}$$

With increasing g, the sequence $R_{g1} \subset R_{g2} \subset \ldots$ forms the Morse filtration. Each new R_g includes the previous one, which allows the study of how the topology of the data evolves. To track the change in the number of connected components, the zeroth Betti number $\beta_0(R_g)$. is used. This number indicates the number of connected parts of the sublevel set R_g. When a local minimum g_i is reached, the sublevel set gains a new connected component:

$$\beta_0(R_{gi-eps}) = \beta_0(R_{gi}) + 1, \tag{8}$$

where eps is a small value. A new component is "born" at the point g_i.

When a local maximum M_i is reached, two connected components merge into one:

$$\beta_0(R_{Mi-eps}) = \beta_0(R_{Mi}) - 1. \tag{9}$$

For matching births and deaths, the elder rule is applied. When two components merge as they pass through a maximum h_i, the component that was born later (i.e. corresponds to a greater minimum value) is chosen. Thus, each minimum g_i is paired with a maximum M_j, forming a pair (g_i, M_j). Based on the pairs (g_i, M_j) a birth-death diagram is constructed. The x-axis represents the birth values (g_i), and the y-axis represents the death values (M_j). Each point on the diagram corresponds to a pair (g_i, M_j), characterizing the temporal life of a connected component.

For the determination of matching births and deaths, three layers of the digital twin with an active face, subjected to climatic factors, and three layers not experiencing such influence were selected.

2.7. Results processing

Following tensile and compressive testing, the elastic modulus (Young's modulus) and ultimate tensile strength were calculated for each specimen. All datasets were first assessed for normality using the Jarque–Bera test. Subsequently, an independent two-sample Student's t-test ($\alpha = 0.05$) was applied to evaluate statistically significant differences between experimental groups. If the distribution was not normal, the non-parametric Mann–Whitney U test was used. The significance level was set at $p < 0.05$. For non-normal data, median (Q1, Q3) was reported. Results were visualized using box-and-whisker plots to illustrate distribution trends and outliers.

Principal component analysis (PCA) was used to explore interdependencies between climatic exposure parameters (e.g., solar irradiance, humidity) and the degradation of mechanical properties in the composite material.

2.8. Experimental design

A total of 80 specimens were fabricated. Prior to climatic exposure, 20 specimens (10 for tensile testing and 10 for compression testing) were evaluated to establish baseline mechanical performance. The remaining 60 specimens were allocated equally across three distinct climatic zones for a three-year aging period. Following exposure, all specimens underwent tensile and compressive testing to assess post-aging mechanical behavior.

3. Results

Following three years of environmental aging, the specimens underwent tensile and compressive mechanical testing. Statistical analysis confirmed that mechanical properties in all experimental groups were normally distributed. Statistically significant differences in tensile strength and elastic modulus were annotated with an asterisk (*), while those in compressive properties were denoted by a percentage symbol (%). Fig. 4 illustrates the variation in mechanical characteristics across the three exposure zones.

Statistical analysis revealed that the tensile strength of control specimens differed significantly ($p < 0.05$) from all climate-exposed groups in both tensile and compressive loading regimes. While the tensile elastic modulus exhibited statistically significant deviations from control values across all exposure groups, compressive modulus values showed no such differences. Comparative analysis between exposure zones highlighted distinct mechanical behavior: specimens aged in Area 1 and Area 2 displayed divergent tensile and compressive

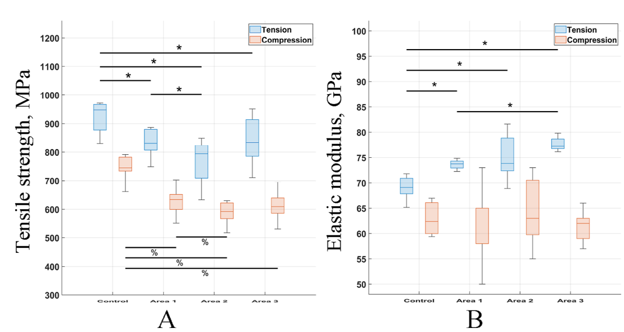

*Fig. 4. Mechanical properties: A — tensile strength, B — elastic modulus; statistically significant results are annotated with symbols: * for tensile, % for compression.*

properties, whereas tensile modulus variations were statistically significant only between Area 1 and Area 3.

Median tensile strength and compressive strength values were 947 MPa and 744 MPa for control specimens, 831 MPa and 633 MPa for Area 1 specimens, 794 MPa and 592 MPa for Area 2 specimens, and 833 MPa and 609 MPa for Area 3 specimens. Median elastic modulus values under tensile and compressive loading were 69 GPa and 62 GPa for control specimens, 73 GPa and 65 GPa for Area 1 specimens, 73 GPa and 63 GPa for Area 2 specimens, and 77 GPa and 62 GPa for Area 3 specimens.

Meteorological data, including annual solar irradiance metrics, are summarized in Fig. 5: total solar radiation (Fig. 5A), UV-A (Fig. 5B), and UV-B (Fig. 5C) activity.

Cumulative solar radiation over the three-year exposure period exhibited statistically significant differences ($p < 0.05$) across all three cities. UV-A radiation intensity diverged significantly between Area 1 and Area 2, while UV-B intensity showed marked variation between Area 1 and Area 3 (Fig. 5A–C).

Mean values for total solar activity were 7150, 4154 and 6106 MJ/m^2; for UV-A 320, 202 and 285 MJ/m^2; and for UV-B 11, 8.3 and 3.9 MJ/m^2 for Area 1, Area 2, and Area 3, respectively.

The study further quantified regional climatic variability. Annual rainfall in Area 2 significantly differed from both Area 1 and Area 3 (Fig. 6A). Mean annual temperatures varied significantly ($p < 0.05$) among all three regions (Fig. 6B). Relative humidity levels in Area 2 were significantly different from those in Area 1 and Area 3 (Fig. 6C). While atmospheric pressure showed no significant differences overall, Area 3 exhibited significantly higher-pressure values compared to the other regions (Fig. 6D).

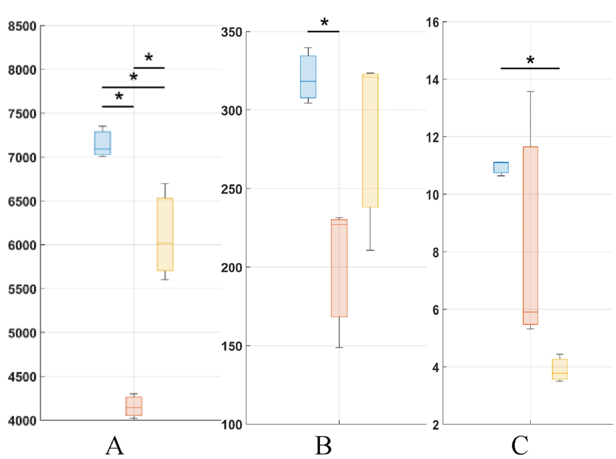

Fig. 5. Solar activity in zones: A – total solar activity, MJ/m^2; B – UV-A activity, MJ/m^2; C – UV-B activity, MJ/m^2; where blue color for Area 1, red color for Area 2, yellow color for Area 3.

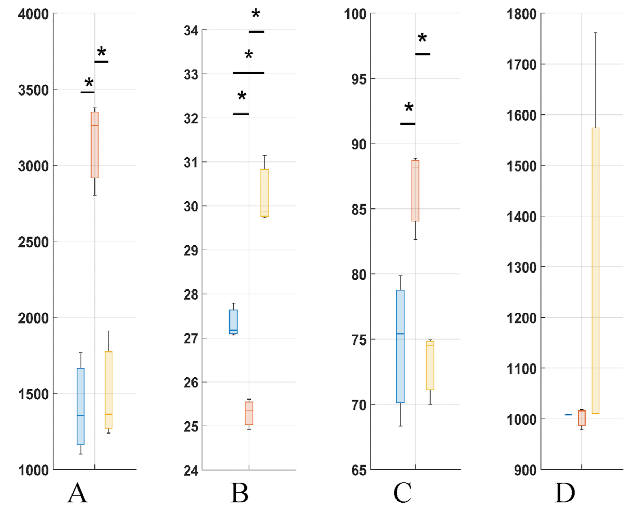

Fig. 6. Weather factors by zones A – total precipitation, mm; B – average temperature, °C; C – average humidity, %; D – average pressure, hPa; where blue color for Area 1, red color for Area 2, yellow color for Area 3.

For Area 1, Area 2, and Area 3, the mean values were obtained as follows: total precipitation – 1408, 3148, and 1504 mm; average temperature – 27.3, 25.3, and 30.3 °C; average humidity – 74, 86, and 73 %; and average pressure – 1008, 1003, and 1260 hPa.

Microscopic evaluation of specimen surfaces revealed distinct structural alterations attributable to environmental exposure. Fig. 7A illustrates the weathered top surface of Area 1-exposed specimens, exhibiting brown discoloration indicative of matrix degradation. In contrast, the protected reverse side (Fig. 7B) displayed localized fiber depigmentation without significant matrix damage.

Area 2-exposed specimens (Fig. 7C) demonstrated similar surface discoloration, with diffuse brown patina confirming matrix deterioration.

Area 1 specimens (Fig. 7D) exhibited pigment loss extending beyond edge regions to span the entire composite segment.

Area 3 specimens (Fig. 7F) showed complete longitudinal depigmentation, suggesting accelerated fiber-matrix interface degradation under sustained tropical conditions.

Analysis of the weathered surface (Fig. 7E) reveals degradation in its incipient phase, characterized by preserved fiber architecture, which is a contrast to advanced degradation observed in prior cases.

PCA identified moisture exposure (loading = 0.64) as the primary driver of mechanical property

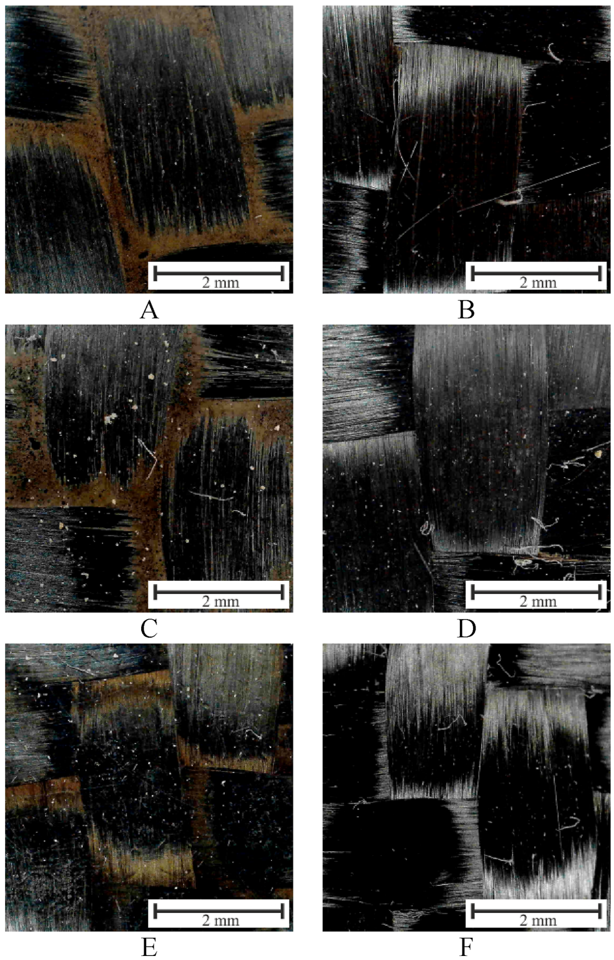

Fig. 7. Specimen surface: A − weathering-exposed surface from Area 1, B − unexposed reverse surface from Area 1, C − weathering-exposed surface from Area 2, D − unexposed reverse surface Area 2, E − weathering-exposed surface from Area 3, F − unexposed reverse surface Area 3.

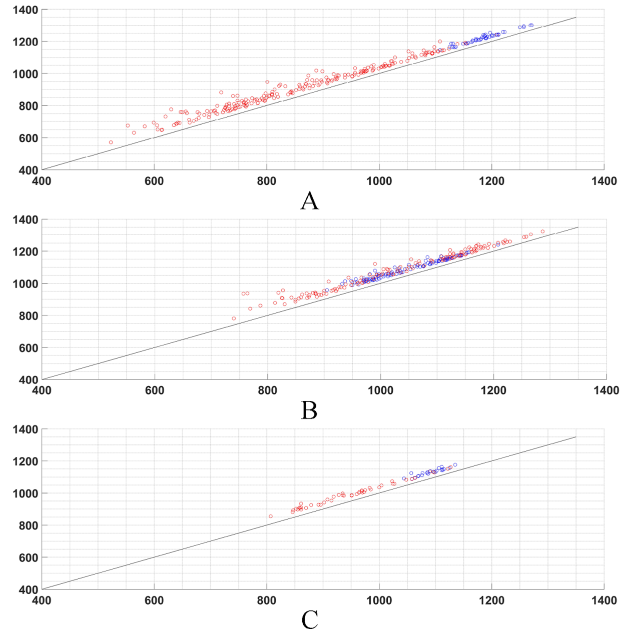

Fig. 8. The birth-death diagram is presented on axes corresponding to Hounsfield values: A − Area 1, B − Area 2, C − Area 3.; red points are unexposed layers, blue points are weathering-exposed layers.

deterioration, followed by UV-B radiation (loading = 0.26). These results underscore the dominant role of hygrothermal conditions in accelerating polymer composite degradation.

The topological analysis, based on the birth-death diagrams, begins with the filtering of the obtained points. The birth and death points were further processed as follows: if the birth and death values were below a predetermined threshold (20 HU), they were excluded from further analysis. All values are expressed in Hounsfield units. The 20 HU threshold for birth-death diagrams was determined from Hounsfield histogram analysis, identifying values below 20 HU as noise or edge effects, where topological features are born and immediately die. Moreover, 20HU difference in optical density is not significant for mechanical properties. For the Area 1 sample (Fig. 8A), a characteristic separation between the weathering-exposed and unexposed layers is observed, which is reflected in the distinct distribution of points on the birth-death diagram. In the Area 2 sample (Fig. 8B), the active and unexposed layers are intermixed, indicating the absence of a clear separation or change in the layer structure. In the Area 3 sample (Fig. 8C), a separation similar to that of Area 1 is present, though it is less pronounced. The line on the diagram, corresponding to a zero lifetime, delineates the boundary between statistically significant and insignificant components.

Additionally, the maximum distance from the zero-lifetime line was evaluated. The maximum distance was 115 HU for Area 1, 125 HU for Area 2, and 51 HU for Area 3.

4. Discussion

Three years of environmental aging induced statistically significant variations in the mechanical properties of specimens across climatic zones. Notably, tensile and compressive strengths diverged significantly between specimens aged in Area 1 and Area 2 ($p < 0.05$), a disparity aligned with elevated UV-A radiation levels (the sole statistically distinct weathering factor between these regions). Similarly, tensile and compressive elastic moduli exhibited significant differences ($p < 0.05$) between Area 1 and Area 3, correlating with divergent UV-B intensity profiles. These findings underscore the critical role of ultraviolet radiation spectra—particularly UV-A and UV-B—in driving region-specific degradation of polymer composites under tropical climatic conditions.

Beyond UV radiation, climatic variables such as cumulative precipitation, mean temperature, and relative humidity also exhibited regional disparities. However, their impact on mechanical performance was secondary to UV-driven degradation. For instance, while Area 2 experienced significantly higher precipitation compared to Area 1 and Area 3 ($p < 0.05$), these differences showed no statistically meaningful correlation with tensile strength or elastic modulus. Similarly, temperature—though varying significantly across all three regions—demonstrated inconclusive effects on material performance, warranting further investigation to elucidate its role in composite aging under tropical conditions.

In [25], epoxy laminates fabricated with Araldite LY-556 resin and HY-951 hardener − a common aerospace-grade composite system − were subjected to 180 h of UV-A radiation ($\lambda = 340$ nm). Post-exposure analysis revealed a 22.6 % reduction in tensile strength, accompanied by surface microcracking and yellowing, indicative of photodegradation. These results underscore the susceptibility of epoxy matrices to UV-A-driven strength degradation, particularly in outdoor applications. Notably, the study also reported a 15 % increase in elastic modulus, attributed to UV-induced post-curing of the polymer network. Similarly, Kumar et al. [26] investigated IM7/997 composites (IM7 carbon fiber/997 thermoplastic-modified epoxy) under combined UV-A and high humidity. The authors observed matrix erosion and mechanical property deterioration, aligning with the hygrothermal degradation mechanisms, the same as in our study. Specifically, both works highlight the synergistic role of UV-A and moisture in reducing tensile and compressive strengths. However, the elastic modulus enhancement reported in Ref. [25] contrasts with typical degradation trends, emphasizing the complex interplay between UV exposure and resin curing kinetics.

The degradation of carbon fiber-reinforced polymer composites under UV-A/B radiation was investigated in Ref. [13], with specimens exposed for 512 h. Results demonstrated an 18.85 % reduction in elastic modulus and a 13.5 % decline in tensile strength due to UV-induced aging. In contrast, our study observed a maximum tensile strength loss of 16.1 %, compressive strength reduction of 20.4 %, and an 11.7 % increase in tensile modulus. These results highlight variations in degradation trends across mechanical properties, potentially linked to differences in material formulations, exposure protocols, or synergistic environmental factors (e.g., humidity).

The results demonstrate that solar radiation components (specifically UV-A and UV-B) are the dominant climatic factors influencing mechanical properties. Thus, UV-A reduces tensile strength and UV-B reduces the elastic modulus. PCA also identifies humidity as a critical factor contributing to the reduction in mechanical properties Other climatic variables have little influence or are masked by the combined effects of UV-A and humidity.

Topological analysis of birth-death diagrams for weathering-exposed and unexposed layers in the composite material reveals a correlation between structural changes and ultraviolet radiation intensity, particularly UV-A. The weathering-exposed and unexposed layers in specimens exposed in Area 2 correlates with the minimal UV-A activity recorded in this region over the three-year expose period. This indicates weakly pronounced structural and mechanical changes in the material, confirmed by the proximity of birth and death points on the diagram and, consequently, the indistinguishability of the layers.

UV-A activity promotes curing of the polymer matrix, which in turn affects the material's strength characteristics, particularly its tensile strength. Similar reasoning applies to specimens from Area 1 and Area 3. The higher UV-A activity and resulting strength properties can be evaluated using the birth-death diagrams.

Additionally, the maximum distance from the zero-lifetime line was assessed. The obtained values were 115 HU for Area 1, 125 HU for Area 2, and 51 HU for Area 3. These data positively correlate with UV-B activity measurements and elastic modulus results, confirming the influence of climatic factors on degradation processes in the composite material.

This study effectively utilized mechanical testing, microscopy, X-ray CT, and topological data analysis to assess composite degradation, but additional analytical techniques could further improve the quality of the analysis. Due to our focus on materials engineering, we did not employ Dynamic Mechanical Analysis (DMA) or nanoindentation to evaluate viscoelastic properties or local hardness gradients, nor X-Ray Diffraction (XRD) to assess crystallinity changes in the polymer matrix, which could elucidate mechanisms behind the 11.7 % modulus increase. Similarly, quantitative void fraction analysis via CT binarization or statistical correlation of topological parameters (e.g., Betti numbers) with mechanical property losses (e.g., 16.1 % tensile strength reduction) was not performed. Future research directions should be prioritized: mechanistic studies to uncover degradation pathways under multifactorial environmental stress; engineering solutions for materials, such as UV-resistant coatings or polymer matrix modifications, to improve long-term durability in harsh climates.

5. Conclusion

The observed reductions in tensile strength (up to 16.1 %) and compressive strength (up to 20.4 %) across all exposure zones indicate significant degradation driven by environmental factors, with UV-A and humidity identified as primary contributors via PCA (loading = 0.64 for moisture, 0.26 for UV-B). The unexpected 11.7 % increase in tensile modulus, particularly in Area 3 (77 GPa vs. 69 GPa for controls), suggests UV-induced post-curing of the polymer matrix, enhancing stiffness but not strength. Microscopy and CT data (Figs. 7 and 8) reveal surface-level degradation (e.g., matrix discoloration, microcracks) and internal structural changes, with birth-death diagrams confirming layer separation in high-UV zones (Area 1: 115 HU, Area 3: 51 HU). A topological analysis indicates weakly pronounced structural and mechanical changes in the material, confirmed by the proximity of birth and death points on the diagram and, consequently, the indistinguishability of the layers. These results highlight the complex interplay of UV radiation and humidity in altering both surface and bulk properties of non-autoclave composites.

Ethical statement

This study does not involve any human participants or animal experiments requiring ethical approval.

Conflicts of interest

The authors of this paper declare that they have no conflicts of interest.

Funding

This research was funded by the subsidy allocated to Kazan Federal University for the state assignment in the sphere of scientific activities, project No. FZSM-2023-0009.

References

[1] Z. Zhang, H. Gao, S. Wen, J. Pang, S. Zhang, C. Cui, Z. Wang, S. Yu, Scalable manufacturing of mechanical robust bioinspired ceramic−resin composites with locally tunable heterogeneous structures, Adv. Mat. 35 (14) (2023) 2209510, https://doi.org/10.1002/adma.202209510.

[2] A. Vinod, J. Tengsuthiwat, R. Vijay, M.R. Sanjay, S. Siengchin, Advancing additive manufacturing: 3D printing of hybrid natural fiber sandwich (Nona/Soy PLA) composites through filament extrusion and its effect on thermo-mechanical properties, Pol. Compos. 45 (9) (2024) 7767−7789, https://doi.org/10.1002/pc.28302.

[3] S. Simões, High-performance advanced composites in multifunctional material design: state of the art, challenges, and future directions, Materials 17 (23) (2024) 5997−6010, https://doi.org/10.3390/ma17235997.

[4] M. McGurk, O. Stodieck, J. Yuan, Probabilistic aeroelastic analysis of high-fidelity composite aircraft wing with manufacturing variability, Comp. Struct. 329 (2023) 117794, https://doi.org/10.1016/j.compstruct.2023.117794.

[5] P. Biswas, M.K. Mondal, Evaluation of a cast AL-MG2SI composite for automobile disk-brake rotor application, J. Mater. Eng. Perform. 33 (2024) 11188−11213, https://doi.org/10.1007/s11665-023-08760-1.

[6] M. Naito, H. Kitamura, M. Koike, H. Kusano, T. Kusumoto, Y. Uchihori, T. Endo, Y. Hagiwara, N. Kiyono, H. Kodama, S. Matsuo, R. Mikoshiba, Y. Takami, M. Yamanaka, H. Akiyama, W. Nishimura, S. Kodaira, Applicability of composite materials for space radiation shielding of spacecraft, Life Sci. Space Res. 31 (2021) 71−79, https://doi.org/10.1016/j.lssr.2021.08.004.

[7] T. Trzepieciński, T. Batu, F. Kibrete, H.G. Lemu, Application of composite materials for energy generation devices, J. Compos. Sci. 7 (2) (2023) 55−70, https://doi.org/10.3390/jcs7020055.

[8] M. Waqar, A.M. Memon, M. Sabih, L.M. Alhems, Composite pipelines: analyzing defects and advancements in non-destructive testing techniques, Eng. Fail. Analys. 157 (2023) 107914, https://doi.org/10.1016/j.engfailanal.2023.107914.

[9] K. Czech, R. Oliwa, D. Krajewski, K. Bulanda, M. Oleksy, G. Budzik, A. Mazurkow, Hybrid polymer composites used in the arms industry: a review, Materials 14 (11) (2021) 3047−3065, https://doi.org/10.3390/ma14113047.

[10] N. Kharin, P. Bolshakov, A.G. Kuchumov, Numerical and experimental study of a lattice structure for orthopedic applications, Materials 16 (2) (2023) 744−760, https://doi.org/10.3390/ma16020744.

[11] P. Bolshakov, A.G. Kuchumov, N. Kharin, K. Akifyev, E. Statsenko, V.V. Silberschmidt, Method of computational design for additive manufacturing of hip endoprosthesis based on basic-cell concept, Int. J. Num. Met. Biomed. Eng. 40 (3) (2024) e3802, https://doi.org/10.1002/cnm.3802.

[12] M.H. Mobarak, Md.A. Islam, N. Hossain, Md.Z.A. Mahmud, Md.T. Rayhan, N.J. Nishi, M.A. Chowdhury, Recent advances of additive manufacturing in implant fabrication − a review, Appl. Surf. Sc. Adv. 18 (2023) 100462, https://doi.org/10.1016/j.apsadv.2023.100462.

[13] W. Tuvayanond, L. Prasittisopin, Design for manufacture and assembly of digital fabrication and additive manufacturing in construction: a review, Buildings 13 (2) (2023) 429−450, https://doi.org/10.3390/buildings13020429.

[14] R. Ghimire, A. Raji, Use of artificial intelligence in design, development, additive manufacturing, and certification of multifunctional composites for aircraft, drones, and spacecraft, Appl. Sci. 14 (3) (2024) 1187−1205, https://doi.org/10.3390/app14031187.

[15] K.N. Akifyev, N. Kharin, E.O. Statsenko, O.A. Sachenkov, P. V. Bolshakov, Pilot study of lattice endoprosthesis buckling by compression in-situ using x-ray tomography, Russ. J.

Biomech. 27 (4) (2023) 32−39, https://doi.org/10.15593/RJBiomech/2023.4.03.
[16] T.B. Hudson, P.J. Follis, J.J. Pinakidis, T. Sreekantmurthy, F. L. Palmieri, Porosity detection and localization during composite cure inside an autoclave using ultrasonic inspection, Compos. Part A: Appl. Sci. Manuf. 147 (2021) 106337, https://doi.org/10.1016/j.compositesa.2021.106337.
[17] F.Y. Addou, F. Bourada, A. Tounsi, A.A. Bousahla, K.H. Benrahou, H. Albalawi, Effect of porosity distribution on flexural and free vibrational behaviors of laminated composite shell using a novel sinusoidal HSDT, Arch. Civ. Mech. Eng. 24 (2024) 102, https://doi.org/10.1007/s43452-024-00894-w.
[18] N.V. Kharin, O.V. Gerasimov, P.V. Bolshakov, A.A. Khabibullin, A.O. Fedyanin, M.E. Baltin, T.V. Baltina, O.A. Sachenkov, Technique for determining the orthotropic properties of the bone organ according to computer tomography, Russ. J. Biomech. 23 (3) (2019) 395−402, https://doi.org/10.15593/RJBiomech/2019.3.11.
[19] K.N. Akifyev, E.O. Statsenko, V.V. Smirnova, N.V. Kharin, P. V. Bolshakov, O.A. Sachenkov, Method for studying the porosity of fluid phase samples by x-ray computed tomography under uniaxial compression, PNRPU Mech. Bull. 2 (2023) 11−21, https://doi.org/10.15593/perm.mech/2023.2.02.
[20] P. Bolshakov, N. Kharin, R. Kashapov, O. Sachenkov, Structural design method for constructions: simulation, manufacturing and experiment, Materials 14 (20) (2021) 6064−6080, https://doi.org/10.3390/ma14206064.
[21] P. Bolshakov, N. Kharin, A. Agathonov, E. Kalinin, O. Sachenkov, Extension of the Voronoi diagram algorithm to orthotropic space for material structural design, Biomimetics 9 (3) (2024) 185, https://doi.org/10.3390/biomimetics9030185.
[22] L.I. Garipova, A.S. Batrakov, F.F. Khabibullin, Mechanical characteristics of a product manufactured by the FDM printing, Russ. Aeronaut. 67 (1) (2024) 145−150, https://doi.org/10.3103/S1068799824010173.
[23] T.S. Muzata, A. Gebrekrstos, J.T. Orasugh, S.S. Ray, An overview of recent advances in polymer composites with improved UV-shielding properties, J. Appl. Polym. Sci. 140 (14) (2023) e53693, https://doi.org/10.1002/app.53693.
[24] S.M. Harle, Durability and long-term performance of fiber reinforced polymer (FRP) composites: a review, Structures 60 (2024) 105881, https://doi.org/10.1016/j.istruc.2024.105881.
[25] R. Naveen, M. Kumar, M. Ramesh, R. Abinaya, Prasath, An investigation on effect of ultraviolet (UV) rays on mechanical properties of epoxy laminates, Mater. Today: Proc. (2023), https://doi.org/10.1016/j.matpr.2023.06.257 (in press).
[26] B.G. Kumar, R.P. Singh, T. Nakamura, Degradation of carbon fiber-reinforced epoxy composites by ultraviolet radiation and condensation, J. Compos. Mater. 36 (24) (2002) 2713−2733, https://doi.org/10.1177/002199802761675511.
[27] A. Vedrtnam, D. Gunwant, H. Verma, K. Kalauni, Effect of aging and UV exposure on mechanical properties of natural fiber composites, in: C. Muthukumar, S. Krishnasamy, S.M. K. Thiagamani, S. Siengchin, eds., Aging Effects on Natural Fiber-Reinforced Polymer Composites, Composites Science and Technology, Springer, Singapore. 2022, pp. 189−217, https://doi.org/10.1007/978-981-16-8360-2_11.
[28] A. Afshar, M. Alkhader, C.S. Korach, F. Chiang, Effect of long-term exposure to marine environments on the flexural properties of carbon fiber vinylester composites, Compos. Struct. 126 (2015) 72−77, https://doi.org/10.1016/j.compstruct.2015.02.008.
[29] V.I. Pavlenko, V.T. Zabolotny, N.I. Cherkashina, O.D. Edamenko, Effect of vacuum ultraviolet on the surface properties of high-filled polymer composites, Inorg. Mater.: Appl. Res. 5 (2014) 219−223, https://doi.org/10.1134/S2075113314030137.
[30] T. Lu, E. Solis-Ramos, Y. Yi, M. Kumosa, UV degradation model for polymers and polymer matrix composites, Polym. Degrad. Stab. 154 (2018) 203−210, https://doi.org/10.1016/j.polymdegradstab.2018.06.004.
[31] C. Cerbu, H. Wang, M.F. Botis, Z. Huang, C. Plescan, Temperature effects on the mechanical properties of hybrid composites reinforced with vegetable and glass fibers, Mech. Mater. 149 (2020) 103538, https://doi.org/10.1016/j.mechmat.2020.103538.
[32] T. Yimyai, D. Crespy, A. Pena-Francesch, Self-healing photochromic elastomer composites for wearable UV-sensors, Adv. Funct. Mater. 33 (20) (2023) 2213717, https://doi.org/10.1002/adfm.202213717.
[33] Y. Sun, S. Yuan, W. Fan, D. Lin, K. Zhang, Z. Bai, Y. Zhu, H. Wang, A smart composite coating with photothermal response, anti-UV and anti-corrosion properties, Chem. Eng. J. 452 (2022) 138983, https://doi.org/10.1016/j.cej.2022.138983.
[34] M. Koo, PH-STAT, arXiv preprint (2025), https://doi.org/10.48550/arXiv.2304.05912, 2304.05912 (in press).
[35] V. Smirnova, E. Semenova, V. Prunov, R. Zamaliev, O. Sachenkov, Topological approach for material structure analyses in terms of R2 orientation distribution function, Mathematics 11 (12) (2023) 2639, https://doi.org/10.3390/math11122639.